

Local high chirality near exceptional points based on asymmetric backscattering

Jingnan Yang,¹ Hancong Li,¹ Sai Yan,² Qihuang Gong,¹ and Xiulai Xu^{1,3,*}

¹*State Key Laboratory for Mesoscopic Physics and Frontiers Science Center for Nano-optoelectronics,
School of Physics, Peking University, 100871 Beijing, China*

²*Beijing National Laboratory for Condensed Matter Physics,*

Institute of Physics, Chinese Academy of Sciences, Beijing 100190, China

³*Peking University Yangtze Delta Institute of Optoelectronics, Nantong, Jiangsu 226010, China*

(Dated: October 8, 2024)

Abstract

We investigate local high chirality inside a microcavity near exceptional points (EPs) achieved via asymmetric backscattering by two internal weak scatterers. At EPs, coalescent eigenmodes exhibit position-dependent and symmetric high chirality characteristics for a large azimuthal angle between the two scatterers. However, asymmetric mode field features appear near EPs. Two azimuthal regions in the microcavity classified by the scatterers exhibit different wave types and chirality. Such local mode field features are attributed to the symmetries of backscattering in direction and spatial distribution. The connections between the wave types, the symmetry of mode field distribution and different symmetries of backscattering near EPs are also analyzed and discussed. Benefiting from the small size of weak scatterers, such microcavities with a high Q/V near EPs can be used to achieve circularly polarized quantum light sources and explore EP modified quantum optical effects in cavity quantum electrodynamics systems.

I. INTRODUCTION

In recent years, optical microcavities have been widely used for studying non-Hermitian physics [1–5]. Exceptional points (EPs) are one of the most significant topics in non-Hermitian physics [6–9], at which eigenstates coalesce with identical eigenfrequencies. For whispering gallery mode (WGM) microcavities, two methods are usually used to achieve EPs. One is based on parity-time (PT) symmetry using balanced loss and gain [10–12]. The other is based on non-reciprocal interactions via asymmetric mode coupling induced by two nanoscat- terers [13, 14] or a perfect reflection mirror [3, 15]. So far, benefiting from the high-sensitivity to perturbations or chiral behaviors at EPs [16, 17], many applications have been reported, such as high-sensitivity detection [18–20], chiral lasing [21, 22] and chiral absorption [23, 24].

Quantum light sources with specific polarization using single quantum emitters (QEs) are in great demand for applications in quantum information and quantum metrology [25, 26]. The single QE is usually weakly coupled with a microcavity to enhance the spontaneous emission rate for improving the brightness and indistinguishability of emitted single photons, and to modify the emission direction and polarization based on the Purcell effect [26–29] and spin-momentum locking effect [30–32]. Due to the nanoscale of a QE, its emission properties are locally decided by the electric field intensity and degree of circular polarization (DCP) where it's located instead of by global properties of cavity modes. Chiral optical modes at EPs have the potential of achieving circularly polarized single-photon sources [33]. However, the application is limited by a low ratio of quality (Q) factor to mode volume (V) of the cavity at EPs. In fact, to

exactly obtain EPs in experiment is nearly impossible which conflicts with the fact that EPs are sensitive to perturbations [34]. Therefore, it's important to obtain a microcavity with a high Q/V and explore the mode field features near EPs, such as the distribution features of electric field and DCP.

Through designing and integrating two nanoscale holes as weak scatterers to induce controllable asymmetric backscattering, microcavities with both non-Hermitian designs and a high Q/V can be obtained [20] for realizing EP enhanced circularly polarized single-photon emission or low-threshold chiral lasing [35] and for studying light-matter interactions near EPs at the quantum level [36–44]. Due to the modification of scatterers, the microcavity exhibits standing-wave features under symmetric backscattering or traveling-wave features at EPs with totally asymmetric backscattering, corresponding to orthogonality or coalescence of cavity modes. This indicates the connection between the wave types and the symmetry of backscattering in direction.

Here we study the mode field features of microcavities near EPs through numerical simulations. The EPs are achieved via asymmetric backscattering induced by two different weak scatterers integrated into a microdisk. Symmetrical mode field features in two azimuthal regions classified by the two scatterers and position-dependent high chirality up to ± 1 are observed at EPs when the two azimuthal regions have similar areas. Asymmetric mode field features are observed near EPs, where the two azimuthal regions exhibit different features in wave type and chirality. The asymmetric and local mode field features are induced by the asymmetry of backscattering in two azimuthal regions and the difference of decay rates for traveling and standing waves, and are differently affected by the scatterer parameters. This work reveals that the wave types and chirality inside the cavity are locally decided by the symmetry of backscattering in di-

* xlxu@iphy.ac.cn

rection, while the asymmetry of backscattering in spatial distribution results in local and asymmetric mode field features.

II. SIMULATIONS AND DESIGN

An unperturbed WGM microcavity has two degenerate cavity modes, propagating along clockwise (CW) or counter-clockwise (CCW) direction, respectively, namely, CW or CCW mode. Such a symmetric microcavity is very sensitive to perturbations like particles, which scatter the light and cause non-Hermitian mode coupling between CW and CCW modes. According to a simplified Hamiltonian picture of a microcavity perturbed by two weak scatterers [13], the backscattering of light from CW to CCW or from CCW to CW direction can be constructively canceled for proper scatterer parameters in size, location and refractive index, corresponding to two different EPs with coalescent CCW or CW modes and totally asymmetric backscattering, respectively.

In principle, a larger overlap between the scatterer and the mode field usually causes a larger mode coupling and a large decay rate. To achieve EPs in a microcavity with high Q/V, we design two slightly different nanoscale air holes in size and location as weak scatterers with the mirror symmetry breaking in the microdisk. As shown in Fig. 1(a), two air holes are designed into a microdisk with five parameters r_1 , d_1 , r_2 , d_2 and β . β is mathematically expected to satisfy $\beta \approx (N + 1/2)\pi/m$ to cancel the scattering from CW to CCW or from CCW to CW direction depending on the backscattering parameters [13]. m is the azimuthal mode number. N is an integral ($N < m$). We use two-dimensional simulation based on the finite element method. The microdisk with a radius of 1 μm is surrounded by an air layer and then a perfectly matched layer both with the depth larger than $\lambda/2$. The maximum mesh is 10 nm, about $\lambda/38$. The material is GaAs with an effective refractive index about 3.0377.

By changing the five parameters of the air holes, the mode coupling strength and the symmetry of backscattering in direction are controlled, as well as the eigenvalues and the wave types of cavity modes. We first consider a large β with $N = 11$ and $m = 12$, where two azimuthal regions have similar areas. Through optimizing the parameters, as shown in Fig. 1(a) and (c), two different EPs, labeled as EP_1 and EP_2 , are obtained respectively, where coalescent modes exhibit traveling wave like features with vague nodes in the distribution of $|E|$. We then investigate the effects of β , r_2 and d_2 on the eigenvalues near EPs. The response of eigenvalues to β is slightly asymmetric near EPs as shown in Fig. 1(e)-(f), while that to r_2 or d_2 is highly asymmetric as shown in Fig. 1(g)-(j). For example, the resonance frequencies (real parts of eigenvalues) and the decay rates (imaginary parts of eigenvalues) for EP_1 have similar values when $r_2 > r_2^{EP}$ and $r_2 < r_2^{EP}$, respectively. These eigen-

frequency features are quite similar to those of coupled microcavities in the exact PT and PT broken phase as a function of the coupling strength g between two microcavities [45].

III. HIGH CHIRALITY AT EPs

Because of the nanoscale size of a QE, the DCP value locally determines the emission polarization of the QE. Therefore, we investigate the DCP distribution in a microcavity at EPs. The normalized DCP is defined as $2\Im[ExEy^*]/(ExEx^* + EyEy^*)$ [33], which describes the differences of Ex and Ey components in phase and amplitude. Here DCP of ± 1 represents left/right circular polarization while DCP of 0 represents linear polarization. As shown in Fig. 1(b), two cavity modes exhibit identical DCP distributions at EP_1 , where a ring-shape region in dark blue inside the microdisk and some outer region surrounding the microcavity exhibit DCP close to -1. Inwards, the DCP along a diameter of the microcavity decreases fast to zero and then increases almost up to 1 (see blue dots in Fig. 5(f)). Outwards, the regions surrounding the microcavities exhibit high chirality, indicating the high chirality remains in the evanescent coupling using a waveguide. For EP_2 , as shown in Fig. 1(d), the cavity modes exhibit the opposite DCP characteristics. To be noted, some regions though exhibiting high chirality can be ignored because the mode field amplitude is too low. Here cavity modes at EP_1 and EP_2 exhibit relatively symmetric features in both $|E|$ and DCP distributions, which are different from EPs realized by two strong (larger size) scatterers with local and asymmetric mode field features [46].

IV. LOCAL MODE FIELD FEATURES NEAR EPs

EPs are critical points in the parameter space, which are technically impossible to exactly reach in experiments. Therefore, we focus on the electric field $|E|$ and DCP distributions near EPs from the perspective of application. When analyzing the mode field distributions near EP_1 , we find the mode field distributions are asymmetric in some cases, which are divided into two azimuthal regions of β and $2\pi - \beta$ with different wave types and chirality by the two scatterers. To quantitatively describe such asymmetric features, we analyze $|E|$ and DCP of two modes distributed in the azimuthal regions of β and $2\pi - \beta$ along a circle inside the microcavity with a radius r_{detect} of 820 nm and 940 nm, respectively. Here $|E|$ and DCP have the maximum values at 820 nm and 940 nm at EP_1 , respectively. When approaching EPs, the cavity modes will start exhibiting partly traveling wave features, where the difference between $|E|$ at antinode and node decreases. To quantify the wave type, we use the cost func-

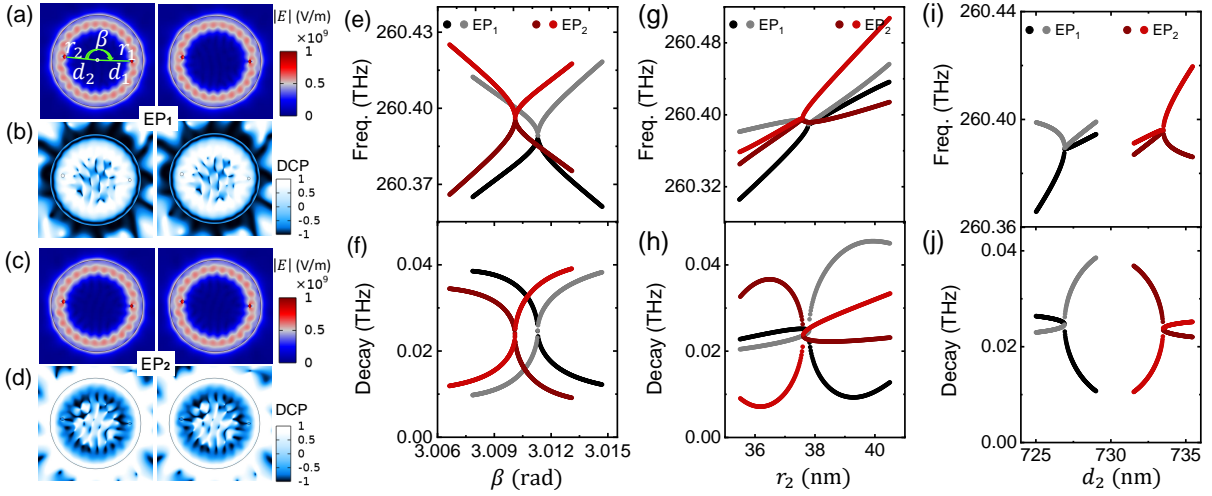


FIG. 1. (a-b) Distributions of electric field $|E|$ (a) and DCP (b) of two modes at EP_1 . (c-d) Distributions of electric field $|E|$ (c) and DCP (d) of two modes near EP_1 and EP_2 (red) when changing β (e)-(f), r_2 (g)-(h) and d_2 (i)-(j), respectively. The parameters for EP_1 and EP_2 are $r_1^{EP} \approx 32.0$ nm, $d_1^{EP} \approx 753.8$ nm, $r_2^{EP} \approx 37.8$ nm, $d_2^{EP} \approx 726.9$ nm and $\beta^{EP} \approx 3.0112924$, and $r_1^{EP} \approx 31.4$ nm, $d_1^{EP} \approx 753.8$ nm, $r_2^{EP} \approx 37.6$ nm, $d_2^{EP} \approx 733.5$ nm and $\beta^{EP} \approx 3.01009295$, respectively.

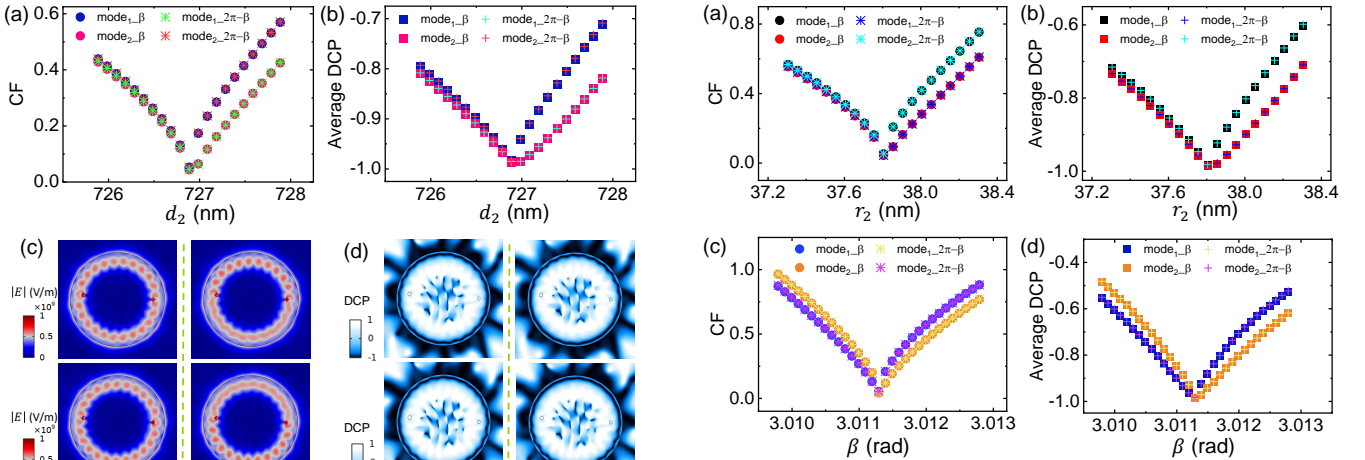


FIG. 2. Local characteristics of electric field $|E|$ and DCP of cavity modes when scanning d_2 near EP_1 . (a)-(b) Cost function (CF) (a) and average DCP (b) of the cavity modes distributed along a circle of $r_{detect} = 820$ nm and a circle of $r_{detect} = 940$ nm in azimuthal regions of β and $2\pi - \beta$ when changing d_2 , respectively. (c)-(d) Typical cases for $|E|$ (c) and DCP (d) distributions of two modes for $d_2 < d_2^{EP}$ and $d_2 > d_2^{EP}$, respectively.

tion (CF) based on the wave envelope and defined as $CF = (|E|_{antinode} - |E|_{node}) / (|E|_{antinode} + |E|_{node})$ [47]. $CF = 0$ and $CF = 1$ correspond to pure traveling waves and pure standing waves, respectively, while $0 < CF < 1$ corresponds to the hybrid waves with a combination of both traveling and standing waves. $|E|_{antinode}$ and $|E|_{node}$ are obtained through sine fitting $|E|$ in the same azimuthal regions. To quantify the chirality, DCP

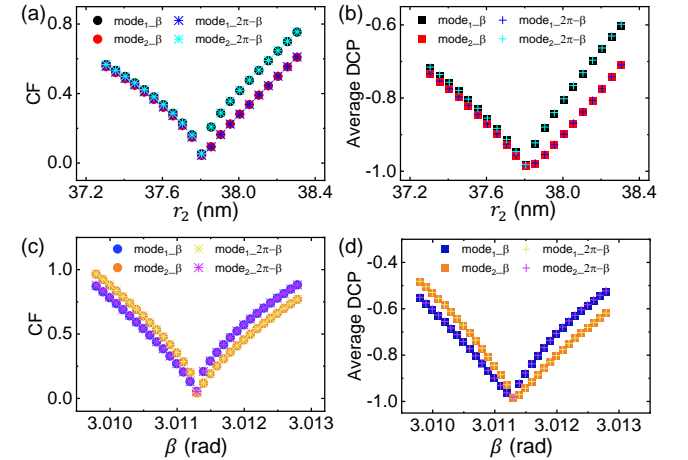


FIG. 3. Local characteristics of $|E|$ and DCP of cavity modes distributed along a circle of $r_{detect} = 820$ nm and a circle of $r_{detect} = 940$ nm in different azimuthal regions when scanning r_2 and β near EP_1 , respectively. (a)-(b) CF (a) and average DCP (b) of cavity modes when changing r_2 . (c)-(d) CF (c) and average DCP (d) of cavity modes when changing β .

values for azimuthal regions of β and $2\pi - \beta$ are respectively averaged along the radians of $r_{detect} = 940$ nm.

Figure 2(a)-(b) show that CF (a) and average DCP (b) in two different azimuthal regions are symmetric for $d_2 < d_2^{EP}$ but asymmetric for $d_2 > d_2^{EP}$, where the differences of CF and DCP values between β azimuthal region (circles) and $2\pi - \beta$ azimuthal region (stars) are very small (see mode field distribution in Fig. 2(c) and (d) for $d_2 < d_2^{EP}$), while CF and average DCP of both modes are different in β azimuthal region and $2\pi - \beta$ azimuthal

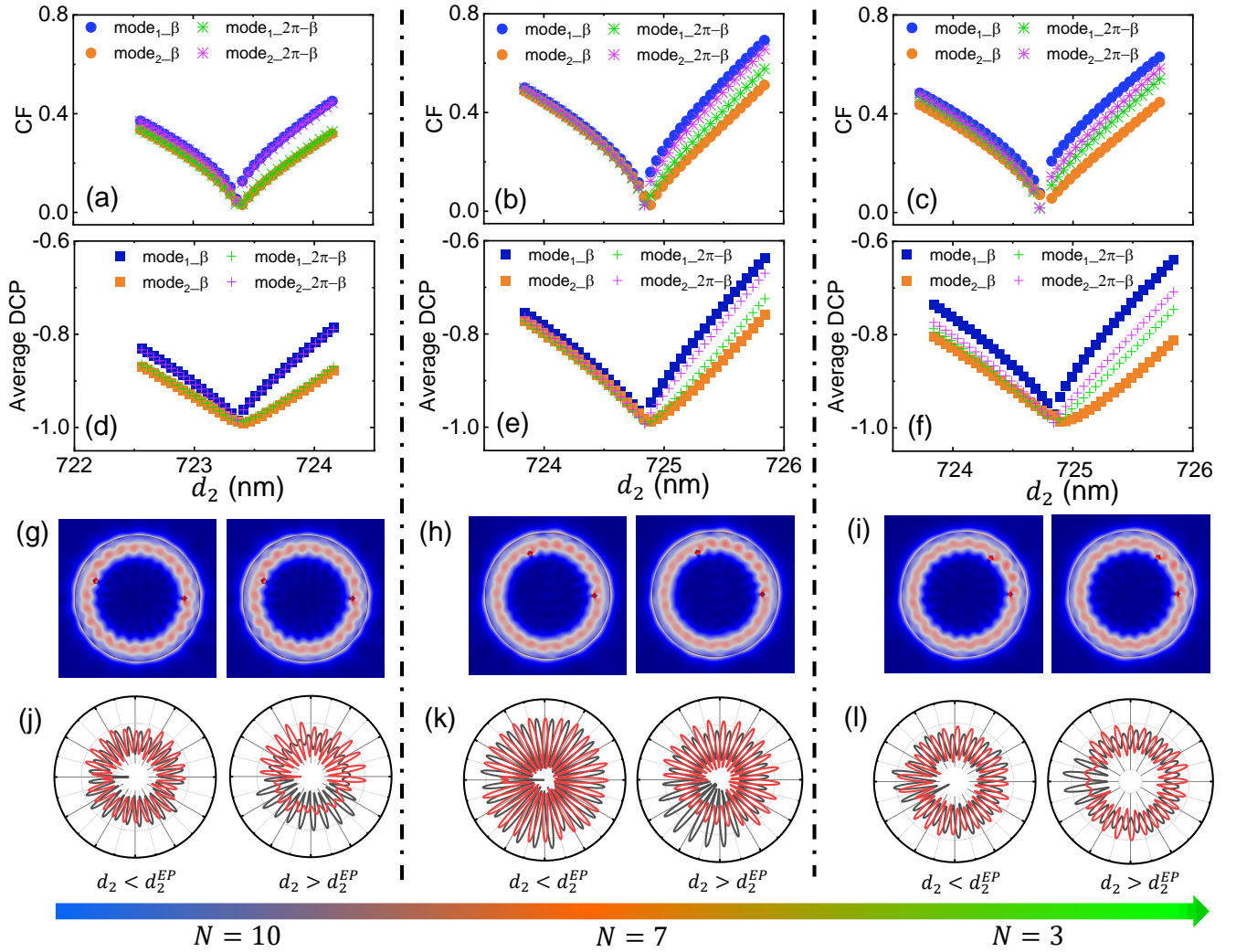


FIG. 4. Local characteristics of $|E|$ and DCP of cavity modes when scanning d_2 near EPs with different N . (a)-(f) CF (a-c) and average DCP (d-f) of the cavity modes for $N = 10, 7, 3$, respectively. (g)-(i) $|E|$ distributions of two cavity modes at EPs for $N = 10, 7, 3$, respectively. (j)-(l) Polar maps of $|E|$ along a circle of $r_{detect} = 820$ nm for $d_2 < d_2^{EP}$ and $d_2 > d_2^{EP}$.

region for $d_2 > d_2^{EP}$ (see mode field distribution in Fig. 2(c) and (d) for $d_2 > d_2^{EP}$). Specifically, DCP in Fig. 2(d) is distributed similarly for $d_2 < d_2^{EP}$ with the similar wave type, but distributed more smoothly only in β or $2\pi - \beta$ azimuthal region with more traveling wave features for $d_2 > d_2^{EP}$. Interestingly, the symmetry of mode field feature is closely related to the decay rates of the cavity modes. The cavity modes exhibiting symmetric mode field features usually have similar decay rates, while the cavity modes with β ($\beta < 2\pi - \beta$) azimuthal region exhibiting a higher CF (less traveling-wave like) always has a larger decay rate. This is because the traveling waves are a little worse confined compared to standing waves, resulting in a larger loss rate for the cavity mode with a lower CF in $2\pi - \beta$ azimuthal region. Usually the decay rates of two cavity modes are much more different for $d_2 > d_2^{EP}$ compared to $d_2 < d_2^{EP}$ as shown in Fig. 1(g)-(j), which explains why the two cavity modes always exchange wave types in two azimuthal regions for

$N = 11$. Apparently, a higher CF usually corresponds to a lower $|DCP|$, through comparing CF and DCP in two azimuthal regions for $d_2 > d_2^{EP}$ in Fig. 2(a) and (b).

Wave types and chirality features when changing r_2 and β are also studied. As shown in Fig. 3(a) and (b), r_2 has similar effects on CF and average DCP to d_2 , while cavity modes for both $\beta > \beta^{EP}$ and $\beta < \beta^{EP}$ exhibit slightly asymmetric mode field features as shown in Fig. 3(c) and (d), which are consistent to the change of two decay rates in Fig. 1(f) where the decay rates are slightly different for $\beta_{EP} < \beta$ and $\beta_{EP} > \beta$ compared to those for d_2 and r_2 in Fig. 1(h) and (j). Compared to the effects of d_2 and r_2 , when change β near β^{EP} , the areas of two azimuthal regions change oppositely. Therefore, the sign of the decay rate difference exchanges near EP_1 when changing β , and the CF and DCP exchange accordingly in different azimuthal regions. In a word, the asymmetric field features in a microcavity with two scatterers near EPs are closely related to the decay rates because trav-

eling waves and standing waves decay differently in the microcavity.

For $N = 11$, the areas of two azimuthal regions are quite similar. To further explore the connections between the wave types, local features of mode field and the asymmetry of azimuthal region area. We consider $TE_{1,12}$ near EPs with different N . As shown in Fig. 4(a)-(f), as N decreases, the differences between CF at β azimuthal region (circles) and $2\pi - \beta$ azimuthal region (stars) increase as well as DCP. The β azimuthal region has a higher CF with more standing-wave like features, as shown in Fig. 4(g)-(i). The small value of β will directly increase the difference between CF in two azimuthal regions, due to the different scattering amplitudes of two scatterers in two azimuthal regions [46]. Such local features between two regions can also be observed for $d_2 > d_2^{EP}$ when decreasing N . As shown in Fig. 4(j)-(l), for $d_2 > d_2^{EP}$, the differences of CF and DCP in $2\pi - \beta$ azimuthal region between two cavity modes decrease. For $d_2 < d_2^{EP}$, the differences of CF and DCP between β azimuthal region and $2\pi - \beta$ azimuthal region increase.

For comparison, the mode field distributions of $TM_{1,12}$ mode at an EP with $m = 12$ and $N = 11$ when scanning d_2 are also analyzed. As shown in Fig. 5(a), asymmetric mode field features in wave type and chirality in two azimuthal regions are relatively less obvious than $TE_{1,12}$ mode in Fig. 2(a). The polar maps of $|E|$ along a circle of $r_{detect} = 820$ nm are relatively symmetric in two azimuthal regions for both $d_2 < d_2^{EP}$ and $d_2 > d_2^{EP}$ as shown in Fig. 5(c). Compared to TE modes, TM modes are a little worse confined and distributed more approaching the microcavity edge as shown by $|E|$ distributions of coalescent cavity modes at EP in Fig. 5(b). Therefore, the scatterers have a relatively smaller overlap with the mode field, which results in weaker backscattering and less asymmetric mode field features [46]. To further demonstrate that the high chirality of mode field results from EPs, $|E|$ and DCP distributions for a microcavity with two identical air holes are also calculated. The cavity modes exhibit obvious standing-wave-like features with distinguishable antinodes and nodes in mode field distributions as shown in Fig. 5(d) and DCP with a low average value close to 0 as shown in Fig. 5(e).

V. DISCUSSION

For PT -symmetry coupled microcavity systems, PT broken phase corresponds to the case with identical resonance frequencies but different decay rates and mode fields distributed asymmetrically in two microcavities, indicating the PT symmetry breaking of eigenstates. While PT unbroken phase corresponds to the case with identical decay rates but different resonance frequencies and the mode field distributed symmetrically in two microcavities [11, 48]. For the single microcavity with asymmetric backscattering in this work, eigenvalue features are similar to those in PT symmetry and PT broken

phase as shown in Fig. 1(g)-(j). Meanwhile, asymmetrical and local features are observed in spatial distribution of $|E|$ and DCP, similar to the spatial field distribution asymmetry in the PT broken phase which are closely related to complex eigenvalues. The PT symmetry breaking with the loss or the gain larger than the coupling strength g is exhibited in asymmetric mode field intensity of two modes in two microcavities. For a microcavity with asymmetric backscattering, the symmetry breaking lies in the asymmetry of backscattering in two azimuthal regions divided by the two scatterers and is exhibited by asymmetric mode features in wave type and chirality in two different azimuthal regions. The dependence of the exchange of asymmetric mode field features in two azimuthal regions between two modes on the decay rates is because traveling waves decay faster than standing waves. Such eigenfrequency-related phenomena reveal the similarities and differences between non-Hermitian optical systems near EPs realized by different methods, and demonstrate that the wave types can be locally controlled in multiple-scatterer physical systems.

Through comparing the distributions of $|E|$ and DCP at EPs, it can be found that the maximum $|DCP|$ is mismatched with the maximum $|E|$. We extract the electric field amplitude $|E|$ and the DCP value of two modes along with a diameter of the microcavity. As shown in Fig. 5(f), the maximum value of $|E|$ corresponds to $DCP=0$. The maximum value of $|DCP|$ corresponds to the location deviating outwards from the mode field antinode, where $|E|$ reduced to 2/3 of the maximum value but still can enable a high cavity enhancement of emission from a QE, carrying specific circular polarization. Both DCP and $|E|$ are position-dependent, therefore, a balance between them needs to be considered according to the expectations of obtaining the highest $|DCP|$ or the highest cavity enhancement for the QE. To further demonstrate the advantages of the high Q/V for our microcavity designs with two weak scatterers, Purcell factor of a dipole located at one antinode in mode field near an EP is calculated using three dimensional simulation based on finite-difference time-domain method. The microdisk is designed with a radius of 1 μm and a thickness of 220 nm. As shown in Fig. 5(g), a Purcell factor up to about 30 is obtained, which is high enough for applications in single-photon sources [26, 49]. So far, EP enhanced emission of a single QE has been theoretically reported [50, 51] but rarely experimentally reported, which is restricted by a large V [52] or a low Q factor [33] for a microcavity at/near an EP. The microcavity with such non-Hermitian designs in this work can be used to explore EP modified quantum effects in cavity QED systems, such as Petermann effect [53], and to realize single-photon sources carrying specific polarization [54].

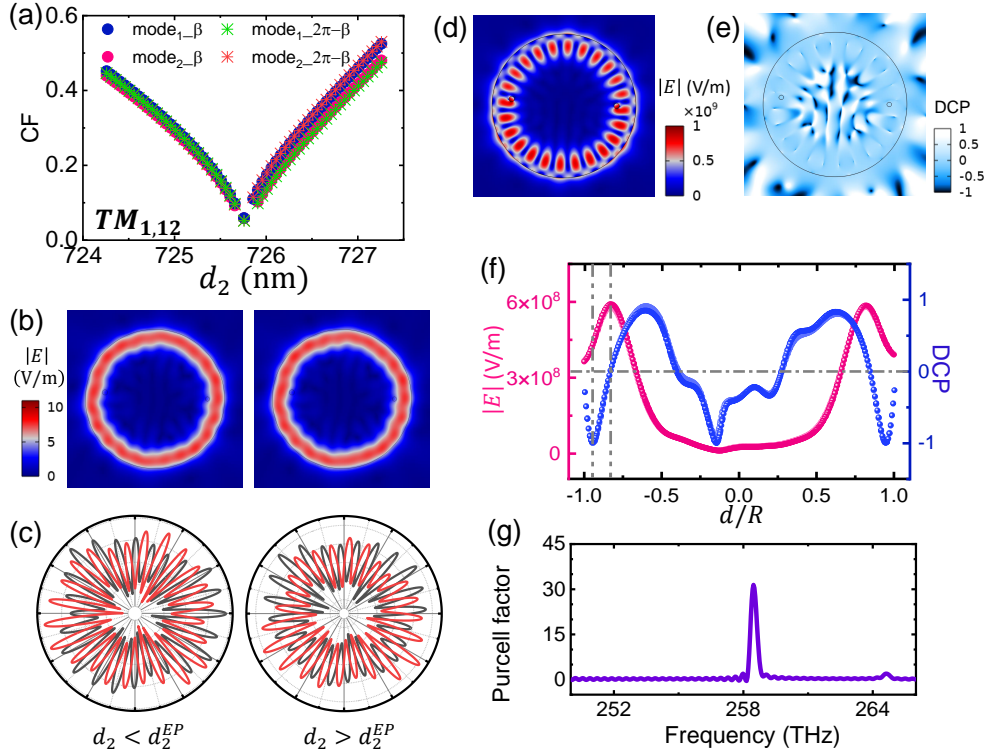


FIG. 5. (a) Characteristics of CF of $TM_{1,12}$ modes near an EP with $N = 11$ when scanning d_2 . (b) $|E|$ distributions of $TM_{1,12}$ modes at EP. (c) Two typical polar maps of $|E|$ for $d_2 < d_2^{EP}$ and $d_2 > d_2^{EP}$ along a circle of $r_{detect} = 820$ nm. (d)-(e) $|E|$ (d) and DCP (e) distributions of $TE_{1,12}$ mode of a microdisk with two identical air holes of $r_1 = r_2 \approx 37.8$ nm, $d_1 = d_2 \approx 726.9$ nm and $\beta \approx 3.0112924$. (f) DCP and $|E|$ along a diameter inside the microcavity from Fig. 1(a)-(b). (g) Purcell factor of a dipole in a microcavity near an EP at an antinode for the mode field.

VI. CONCLUSION

In summary, we study the symmetry of mode field features in wave types and chirality of cavity modes in a microcavity with asymmetric backscattering at/near EPs induced by two different weak nanoscaters. Our results show that cavity modes at EPs exhibit very high chirality which is position-dependent. We also observe asymmetric mode field features in wave type and chirality of two azimuthal regions divided by the two scatterers near EPs. The asymmetry in the areas of two azimuthal regions will further strengthen the asymmetric mode field features while a weaker scattering can weaken the asymmetric features. The asymmetric field features near EPs are eigenfrequency related, attributed to the asymmetry of backscattering in two azimuthal regions and the different decay rates of traveling waves and standing waves. Furthermore, a Purcell factor up to 30 is obtained for the microdisk near an EP. Our work helps deeper understand how the symmetries of backscattering in direction and spatial distribution affect the wave type, chirality and the symmetry of mode field distribution in

non-Hermitian multiple-scattering processes, and demonstrates that wave types and chirality can be locally controlled. Benefiting from the small size of air holes, microcavities with high Q/V near EPs can be obtained for studying EP modified quantum effects in cavity QED systems and realizing chiral quantum light sources with highly circular polarization.

VII. ACKNOWLEDGMENTS

This work was supported by the National Key Research and Development Program of China (Grant No. 2021YFA1400700), the National Natural Science Foundation of China (Grants Nos. 62025507, 11934019, 92250301 and 12204020), China Postdoctoral Science Foundation (Grant No. 2022M710234).

VIII. COMPETING INTERESTS

The authors declare no competing interests.

[1] W. D. Heiss, The physics of exceptional points, *J. Phys. A Math.Theor.* **45**, 444016 (2012).

[2] M.-A. Miri and A. Alù, Exceptional points in optics and photonics, *Science* **363**, eaar7709 (2019).

- [3] Q. Zhong, S. Ozdemir, A. Eisfeld, A. Metelmann, and R. El-Ganainy, Exceptional-point-based optical amplifiers, *Phys. Rev. Appl.* **13**, 014070 (2020).
- [4] W. Li, R. Liu, J. Li, J. Zhong, Y.-W. Lu, H. Chen, and X.-H. Wang, Highly efficient single-exciton strong coupling with plasmons by lowering critical interaction strength at an exceptional point, *Phys. Rev. Lett.* **130**, 143601 (2023).
- [5] D. Anderson, M. Shah, and L. Fan, Clarification of the exceptional-point contribution to photonic sensing, *Phys. Rev. Appl.* **19**, 034059 (2023).
- [6] W. D. Heiss, Exceptional points of non-hermitian operators, *Journal of Physics A: Mathematical and General* **37**, 2455 (2004).
- [7] E. J. Bergholtz, J. C. Budich, and F. K. Kunst, Exceptional topology of non-hermitian systems, *Rev. Mod. Phys.* **93**, 015005 (2021).
- [8] K. Kawabata, T. Bessho, and M. Sato, Classification of exceptional points and non-hermitian topological semimetals, *Phys. Rev. Lett.* **123**, 066405 (2019).
- [9] A. Li, H. Wei, M. Cotrufo, W. Chen, S. Mann, X. Ni, B. Xu, J. Chen, J. Wang, S. Fan, C.-W. Qiu, A. Alù, and L. Chen, Exceptional points and non-hermitian photonics at the nanoscale, *Nature Nanotechnology* **18**, 706 (2023).
- [10] L. Feng, R. El-Ganainy, and L. Ge, Non-Hermitian photonics based on parity–time symmetry, *Nat. Photonics* **11**, 752 (2017).
- [11] R. El-Ganainy, K. G. Makris, M. Khajavikhan, Z. H. Musslimani, S. Rotter, and D. N. Christodoulides, Non-Hermitian physics and PT symmetry, *Nat. Phys.* **14**, 11 (2018).
- [12] J. Wiersig, Revisiting the hierarchical construction of higher-order exceptional points, *Phys. Rev. A* **106**, 063526 (2022).
- [13] J. Wiersig, Structure of whispering-gallery modes in optical microdisks perturbed by nanoparticles, *Phys. Rev. A* **84**, 063828 (2011).
- [14] K. Hong and L. Chen, Mie scatterers bring a resonator to an exceptional point, *Light: Science & Applications* **12**, 216 (2023).
- [15] A. Hashemi, K. Busch, D. N. Christodoulides, S. K. Ozdemir, and R. El-Ganainy, Linear response theory of open systems with exceptional points, *Nature Communications* **13**, 3281 (2022).
- [16] Z. G. Yuto Ashida and M. Ueda, Non-hermitian physics, *Advances in Physics* **69**, 249 (2020).
- [17] J. Wiersig, Prospects and fundamental limits in exceptional point-based sensing, *Nature Communications* **11**, 2454 (2020).
- [18] H. Hodaei, A. U. Hassan, S. Wittek, H. Garcia-Gracia, R. El-Ganainy, D. N. Christodoulides, and M. Khajavikhan, Enhanced sensitivity at higher-order exceptional points, *Nature* **548**, 187 (2017).
- [19] Y.-H. Lai, Y.-K. Lu, M.-G. Suh, Z. Yuan, and K. Vahala, Observation of the exceptional-point-enhanced sagnac effect, *Nature* **576**, 65 (2019).
- [20] J. Wiersig, Sensors operating at exceptional points: General theory, *Phys. Rev. A* **93**, 033809 (2016).
- [21] B. Peng, Ş. K. Özdemir, M. Liertzer, W. Chen, J. Kramer, H. Yilmaz, J. Wiersig, S. Rotter, and L. Yang, Chiral modes and directional lasing at exceptional points, *Proc. Natl. Acad. Sci. U.S.A.* **113**, 6845 (2016).
- [22] B. Peng, Ş. K. Özdemir, F. Lei, F. Monifi, M. Gianfreda, G. L. Long, S. Fan, F. Nori, C. M. Bender, and L. Yang, Parity–time-symmetric whispering-gallery microcavities, *Nature Physics* **10**, 394 (2014).
- [23] S. Soleymani, Q. Zhong, M. Mokim, S. Rotter, R. El-Ganainy, and Ş. K. Özdemir, Chiral and degenerate perfect absorption on exceptional surfaces, *Nat. Commun.* **13**, 599 (2022).
- [24] W. R. Sweeney, C. W. Hsu, S. Rotter, and A. D. Stone, Perfectly absorbing exceptional points and chiral absorbers, *Phys. Rev. Lett.* **122**, 093901 (2019).
- [25] J.-W. Pan, Z.-B. Chen, C.-Y. Lu, H. Weinfurter, A. Zeilinger, and M. Żukowski, Multiphoton entanglement and interferometry, *Rev. Mod. Phys.* **84**, 777 (2012).
- [26] H. Wang, Y.-M. He, T.-H. Chung, H. Hu, Y. Yu, S. Chen, X. Ding, M.-C. Chen, J. Qin, X. Yang, R.-Z. Liu, Z.-C. Duan, J.-P. Li, S. Gerhardt, K. Winkler, J. Jurkat, L.-J. Wang, N. Gregersen, Y.-H. Huo, Q. Dai, S. Yu, S. Höfling, C.-Y. Lu, and J.-W. Pan, Towards optimal single-photon sources from polarized microcavities, *Nature Photonics* **13**, 770 (2019).
- [27] X. Xie, W. Zhang, X. He, S. Wu, J. Dang, K. Peng, F. Song, L. Yang, H. Ni, Z. Niu, C. Wang, K. Jin, X. Zhang, and X. Xu, Cavity quantum electrodynamics with second-order topological corner state, *Laser & Photonics Reviews* **14**, 1900425 (2020).
- [28] J. Yang, S. Shi, X. Xie, S. Wu, S. Xiao, F. Song, J. Dang, S. Sun, L. Yang, Y. wang, Z.-Y. Ge, B.-B. Li, Z. Zuo, K. Jin, and X. Xu, Enhanced emission from a single quantum dot in a microdisk at a deterministic diabolical point, *Opt. Express* **29**, 14231 (2021).
- [29] L. Yang, Y. Yuan, B. Fu, J. Yang, D. Dai, S. Shi, S. Yan, R. Zhu, X. Han, H. Li, Z. Zuo, C. Wang, Y. Huang, K. Jin, Q. Gong, and X. Xu, Revealing broken valley symmetry of quantum emitters in wse2 with chiral nanocavities, *Nature Communications* **14**, 4265 (2023).
- [30] P. Lodahl, S. Mahmoodian, S. Stobbe, A. Rauschenbeutel, P. Schneeweiss, J. Volz, H. Pichler, and P. Zoller, Chiral quantum optics, *Nature* **541**, 473 (2017).
- [31] S. Barik, A. Karasahin, S. Mittal, E. Waks, and M. Hafezi, Chiral quantum optics using a topological resonator, *Phys. Rev. B* **101**, 205303 (2020).
- [32] S. Xiao, S. Wu, X. Xie, J. Yang, W. Wei, S. Shi, F. Song, J. Dang, S. Sun, L. Yang, Y. Wang, S. Yan, Z. Zuo, T. Wang, J. Zhang, K. Jin, and X. Xu, Chiral photonic circuits for deterministic spin transfer, *Laser & Photonics Reviews* **15**, 2100009 (2021).
- [33] C. F. Fong, Y. Ota, Y. Arakawa, S. Iwamoto, and Y. K. Kato, Chiral modes near exceptional points in symmetry broken H1 photonic crystal cavities, *Phys. Rev. Res.* **3**, 043096 (2021).
- [34] P. Djourwe, Y. Pennec, and B. Djafari-Rouhani, Exceptional point enhances sensitivity of optomechanical mass sensors, *Phys. Rev. Appl.* **12**, 024002 (2019).
- [35] M. Kim, K. Kwon, J. Shim, Y. Jung, and K. Yu, Partially directional microdisk laser with two Rayleigh scatterers, *Opt. Lett.* **39**, 2423 (2014).
- [36] H.-Z. Chen, T. Liu, H.-Y. Luan, R.-J. Liu, X.-Y. Wang, X.-F. Zhu, Y.-B. Li, Z.-M. Gu, S.-J. Liang, H. Gao, L. Lu, L. Ge, S. Zhang, J. Zhu, and R.-M. Ma, Revealing the missing dimension at an exceptional point, *Nature Physics* **16**, 571 (2020).

- [37] C. Qian, X. Xie, J. Yang, K. Peng, S. Wu, F. Song, S. Sun, J. Dang, Y. Yu, M. J. Steer, I. G. Thayne, K. Jin, C. Gu, and X. Xu, Enhanced strong interaction between nanocavities and p -shell excitons beyond the dipole approximation, *Phys. Rev. Lett.* **122**, 087401 (2019).
- [38] S. Garmon, G. Ordóñez, and N. Hatano, Anomalous-order exceptional point and non-markovian purcell effect at threshold in one-dimensional continuum systems, *Phys. Rev. Res.* **3**, 033029 (2021).
- [39] M. Khanbekyan and J. Wiersig, Decay suppression of spontaneous emission of a single emitter in a high- q cavity at exceptional points, *Phys. Rev. Res.* **2**, 023375 (2020).
- [40] F. Zhang, J. Ren, L. Shan, X. Duan, Y. Li, T. Zhang, Q. Gong, and Y. Gu, Chiral cavity quantum electrodynamics with coupled nanophotonic structures, *Phys. Rev. A* **100**, 053841 (2019).
- [41] A. Pick, Z. Lin, W. Jin, and A. W. Rodriguez, Enhanced nonlinear frequency conversion and purcell enhancement at exceptional points, *Phys. Rev. B* **96**, 224303 (2017).
- [42] C. Qian, S. Wu, F. Song, K. Peng, X. Xie, J. Yang, S. Xiao, M. J. Steer, I. G. Thayne, C. Tang, Z. Zuo, K. Jin, C. Gu, and X. Xu, Two-photon rabi splitting in a coupled system of a nanocavity and exciton complexes, *Phys. Rev. Lett.* **120**, 213901 (2018).
- [43] F. P. Laussy, E. del Valle, and C. Tejedor, Strong coupling of quantum dots in microcavities, *Phys. Rev. Lett.* **101**, 083601 (2008).
- [44] K. Srinivasan and O. Painter, Linear and nonlinear optical spectroscopy of a strongly coupled microdisk-quantum dot system, *Nature* **450**, 862 (2007).
- [45] C. Wang, Z. Fu, W. Mao, J. Qie, A. D. Stone, and L. Yang, Non-hermitian optics and photonics: from classical to quantum, *Adv. Opt. Photon.* **15**, 442 (2023).
- [46] J. Zhu, C. Wang, C. Tao, Z. Fu, H. Liu, F. Bo, L. Yang, G. Zhang, and J. Xu, Local chirality at exceptional points in optical whispering-gallery microcavities, *Phys. Rev. A* **108**, L041501 (2023).
- [47] S. Motaharibidgoli, S. Davaria, V. V. Sriram Malladi, and P. A. Tarazaga, Developing coexisting traveling and standing waves in euler-bernoulli beams using a single-point excitation and a spring-damper system, *Journal of Sound and Vibration* **556**, 117728 (2023).
- [48] C. M. Bender and S. Boettcher, Real spectra in non-hermitian hamiltonians having pt symmetry, *Phys. Rev. Lett.* **80**, 5243 (1998).
- [49] P. Senellart, G. Solomon, and A. White, High-performance semiconductor quantum-dot single-photon sources, *Nature Nanotechnology* **12**, 1026 (2017).
- [50] Y. Lu, Y. Zhao, R. Li, and J. Liu, Anomalous spontaneous emission dynamics at chiral exceptional points, *Opt. Express* **30**, 41784 (2022).
- [51] Y. Lu, H. Tan, and Z. Liao, Dressed bound states at chiral exceptional points, *Phys. Rev. A* **107**, 043714 (2023).
- [52] J. Zhu, Şahin Kaya Özdemir, L. He, and L. Yang, Controlled manipulation of mode splitting in an optical microcavity by two rayleigh scatterers, *Opt. Express* **18**, 23535 (2010).
- [53] A. Pick, B. Zhen, O. D. Miller, C. W. Hsu, F. Hernandez, A. W. Rodriguez, M. Soljačić, and S. G. Johnson, General theory of spontaneous emission near exceptional points, *Opt. Express* **25**, 12325 (2017).
- [54] J. Yang, S. Shi, S. Yan, R. Zhu, X. Zhao, Y. Qin, B. Fu, X. Chen, H. Li, Z. Zuo, K. Jin, Q. Gong, and X. Xu, Non-orthogonal cavity modes near exceptional points in the far field, *Communications Physics* **7**, 13 (2024).